Published in final edited form as:

Cell. 2015 May 7; 161(4): 833–844. doi:10.1016/j.cell.2015.04.011.

Structure of the Angiotensin Receptor Revealed by Serial Femtosecond Crystallography

Haitao Zhang[1], **Hamiyet Unal**[2], **Cornelius Gati**[3], **Gye Won Han**[4], **Wei Liu**[5], **Nadia A. Zatsepin**[6], **Daniel James**[6], **Dingjie Wang**[6], **Garrett Nelson**[6], **Uwe Weierstall**[6], **Michael R. Sawaya**[7], **Qingping Xu**[8], **Marc Messerschmidt**[9], **Garth J. Williams**[10], **Sébastien Boutet**[10], **Oleksandr M. Yefanov**[3], **Thomas A. White**[3], **Chong Wang**[11], **Andrii Ishchenko**[4], **Kalyan C. Tirupula**[2], **Russell Desnoyer**[2], **Jesse Coe**[5], **Chelsie E. Conrad**[5], **Petra Fromme**[5], **Raymond C. Stevens**[1,4,12], **Vsevolod Katritch**[1], **Sadashiva S. Karnik**[2], and **Vadim Cherezov**[4,*]

[1]Department of Biological Sciences, Bridge Institute, University of Southern California, Los Angeles, CA 90089, USA

[2]Department of Molecular Cardiology, Lerner Research Institute, Cleveland Clinic, Cleveland, OH 44195, USA

[3]Center for Free Electron Laser Science, Deutsches Elektronen-Synchrotron DESY, 22607 Hamburg, Germany

[4]Department of Chemistry, Bridge Institute, University of Southern California, Los Angeles, CA 90089 USA

[*]**Correspondence:**cherezov@usc.edu (V.C.).

ACCESSION NUMBERS

The coordinates and structure factors have been deposited into the Protein Data Bank under the accession code 4YAY.

SUPPLEMENTAL INFORMATION

Supplemental Information including three tables, three figures, and extended experimental procedures can be found with this article online.

AUTHOR CONTRIBUTIONS

H.Z. designed, optimized, purified and characterized receptor constructs for structural studies, crystallized the receptor in LCP, collected and processed diffraction data, determined the structure, analyzed the data and wrote the paper. H.U. performed mutagenesis, signaling and ligand binding studies and contributed to writing the paper. C.G. participated in the XFEL data collection and processed XFEL data. G.W.H. solved and refined the AT1R structure. N.A.Z. participated in XFEL data collection and contributed in the XFEL data processing. D.J., D.W., G.N., U.W. designed, prepared and operated the LCP injector during the XFEL data collection. M.M., G.J.W., S.B. operated the CXI beamline and performed the XFEL data collection. O.M.Y. refined the geometry of the CSPAD detector. T.A.W. implemented new data processing algorithms in CrystFEL, used in this study. W.L., C.W. and A.I. helped with XFEL sample preparation and participated in the XFEL data collection. K.C.T. and R.D. participated in mutagenesis, membrane production, signaling and ELISA data collection and analysis. M.R.S. and Q.X. helped with synchrotron data processing, XFEL structure solution and structure validation. J.C., C.E.C. and P.F. helped with biophysical characterization of microcrystals at LCLS and participated in the XFEL data collection. R.C.S. conceived the project, supervised receptor expression and characterization, and contributed to writing the paper. V.K. designed initial AT1R constructs, analyzed the structure, performed docking studies and wrote the paper. S.S.K. conceived the project, supervised mutagenesis and functional studies, and contributed to writing the paper. V.C. conceived the project, supervised crystallization and crystallographic data collection, analyzed the data and wrote the paper. Edits were provided by C.G, G.W.H., T.A.W., U.W. and P.F.

[5]Department of Chemistry and Biochemistry, Center for Applied Structural Discovery at the Biodesign Institute, Arizona State University, Tempe, AZ 85287, USA

[6]Department of Physics, Arizona State University, Tempe, AZ 85287, USA

[7]Department of Chemistry and Biochemistry, the UCLA-DOE Institute for Genomics and Proteomics, University of California, Los Angeles, CA 90095, USA

[8]Joint Center for Structural Genomics, Stanford Synchrotron Radiation Light Source, SLAC National Accelerator Laboratory, Menlo Park, CA 94025, USA

[9]BioXFEL Science and Technology Center, Buffalo, NY 14203, USA

[10]Linac Coherent Light Source, SLAC National Accelerator Laboratory, Menlo Park, CA 94025, USA

[11]Department of Chemistry and Chemical Biology, Harvard University, Cambridge, MA 02138, USA

[12]iHuman Institute, ShanghaiTech University, Shanghai, 201210 China

SUMMARY

Angiotensin II type 1 receptor (AT_1R) is a G protein-coupled receptor that serves as a primary regulator for blood pressure maintenance. Although several anti-hypertensive drugs have been developed as AT_1R blockers (ARBs), the structural basis for AT_1R ligand-binding and regulation has remained elusive, mostly due to the difficulties of growing high quality crystals for structure determination using synchrotron radiation. By applying the recently developed method of serial femtosecond crystallography at an X-ray free-electron laser, we successfully determined the room-temperature crystal structure of the human AT_1R in complex with its selective antagonist ZD7155 at 2.9 Å resolution. The AT_1R-ZD7155 complex structure revealed key structural features of AT_1R and critical interactions for ZD7155 binding. Docking simulations of the clinically used ARBs into the AT_1R structure further elucidated both the common and distinct binding modes for these anti-hypertensive drugs. Our results thereby provide fundamental insights into AT_1R structure-function relationship and structure-based drug design.

INTRODUCTION

Cardiovascular disease remains one of the main causes of death throughout the world despite impressive advances in diagnosis and therapeutics during the past few decades. Hypertension is the most common modifiable risk factor in cardiovascular disease, as myocardial infarction, stroke, heart failure, and renal disease can be greatly reduced by lowering blood pressure (Zaman et al., 2002). The best known regulator of blood pressure is the renin-angiotensin system (RAS). Over-stimulation of the RAS is implicated in hypertension, cardiac hypertrophy, heart failure, ischemic heart disease, and nephropathy (Balakumar and Jagadeesh, 2014). A cascade of proteolytic reactions in the RAS can generate various angiotensin peptides. Renin cleaves the precursor protein, angiotensinogen, releasing the inactive angiotensin I. Subsequently, angiotensin I is cleaved by angiotensin converting enzyme (ACE) to generate angiotensin II (AngII), angiotensin III, and

angiotensin 1–7. These peptides exert diverse functions; angiotensins II and III act as vasoconstrictors, while angiotensin 1–7 acts as a vasodilator (Zaman et al., 2002). AngII is also responsible for cell migration, protein synthesis, endothelial dysfunction, inflammation, and fibrosis (Ramchandran et al., 2006).

In humans, AngII binds to two subtypes of angiotensin G protein-coupled receptors (GPCRs), angiotensin II type 1 receptor (AT_1R) and angiotensin II type 2 receptor (AT_2R) (Oliveira et al., 2007). Almost all physiological and pathophysiological effects of AngII are mediated by AT_1R (de Gasparo et al., 2000), while the function of AT_2R remains largely unknown (Akazawa et al., 2013). AT_1R exhibits multiple active conformations, thereby activating different signaling pathways with differential functional outcomes (Shenoy and Lefkowitz, 2005). The G protein-dependent signaling by AT_1R is vital for normal cardiovascular homeostasis yet detrimental in chronic dysfunction, which associates with cell death and tissue fibrosis, and leads to cardiac hypertrophy and heart failure (Ma et al., 2010). Accumulating evidence suggests that G protein independent β-arrestin mediated signaling by AT_1R confers cardio-protective benefits (Whalen et al., 2011; Wisler et al., 2014).

Targeting the RAS cascade has proven to be effective in the treatment of hypertension, as well as specific cardiovascular and renal disorders. The most commonly used drugs include renin inhibitors, ACE inhibitors, and AT_1R blockers (ARBs). ARBs, or sartans, are non-peptide antagonists and include the well-known anti-hypertensive drugs losartan, candesartan, valsartan, irbesartan, telmisartan, eprosartan, olmesartan, and azilsartan, most of which share a common biphenyl-tetrazole scaffold (Burnier and Brunner, 2000; Imaizumi et al., 2013; Miura et al., 2013a; Miura et al., 2013b). These ARBs are now extensively used for the treatment of cardiovascular diseases, including hypertension, cardiac hypertrophy, arrhythmia, and heart failure. There is additional interest in ARBs regarding their efficacy in the treatment of blood-vessel diseases such as Marfan-like syndrome, aortic dissection, and aortic aneurysms (Keane and Pyeritz, 2008; Ramanath et al., 2009).

Previous functional studies on AT_1R have provided numerous clues into AT_1R activation and inhibition mechanisms (Oliveira et al., 2007). Despite its high medical relevance and decades of research, the structure of AT_1R and the binding mode of ARBs, however, are still unknown, which limits our understanding of the structural basis for AT_1R function and modulation, and precludes the rational optimization of AT_1R lead compounds. One such experimental antihypertensive compound is ZD7155, a high affinity antagonist and precursor to the antihypertensive drug candesartan. ZD7155 has a biphenyl-tetrazole scaffold similar to other ARBs, and is more potent and longer-lasting than the first clinically used ARB losartan (Junggren et al., 1996). While structures of several different GPCRs have been reported, the determination of a new GPCR structure remains a significant challenge. X-ray crystallography using synchrotron radiation requires sufficiently large crystals in order to collect high resolution data. Our extensive efforts to solve the AT_1R structure were hampered by the limited size of micro-crystals grown in the membrane mimetic matrix known as lipidic cubic phase (LCP) (Caffrey and Cherezov, 2009). Nevertheless, by applying the recently developed method of serial femtosecond crystallography with LCP as a growth and carrier matrix for delivering microcrystals (LCP-SFX) into an X-ray free-

electron laser (XFEL) beam (Liu et al., 2013; Weierstall et al., 2014; Liu et al., 2014a), we successfully determined the room-temperature crystal structure of the human AT_1R in complex with ZD7155 (AT_1R-ZD7155). Based on the AT_1R-ZD7155 structure, we further performed mutagenesis and docking simulations to reveal binding modes for clinically used antihypertensive drugs targeting AT_1R.

RESULTS

Structure determination of AT_1R-ZD7155 complex using LCP-SFX method

To facilitate crystallization, a thermostabilized apocytochrome, b_{562}RIL (BRIL) (Chun et al., 2012), was fused to the amino terminus (N-terminus) of the human AT_1R. Eleven residues were truncated from the N-terminal region of AT_1R (Met1, Thr7-Asp16), in order to shorten the flexible N-terminus while keeping both the putative glycosylation site at Asn4 and the disulfide bond site at Cys18 intact. Forty residues were truncated from the carboxyl terminus (C-terminus) after the cytoplasmic helix VIII (Figure 1A). The effect of protein engineering on AT_1R function was evaluated using radio-ligand binding and calcium mobilization assays, in which neither the truncations nor BRIL insertion significantly altered the functional and pharmacological properties of the receptor for ligand binding and signaling (Figure 1B–D). With this engineered AT_1R, we obtained micro-crystals (maximum size 40×4×4 μm^3) in monoolein-based LCP, supplemented with cholesterol (Figure S1A). These microcrystals diffracted to only about 4 Å resolution at a synchrotron source under cryogenic conditions. To improve the resolution and avoid radiation damage and freezing, we took advantage of a recently developed LCP-SFX method and collected diffraction data at room temperature at the Linac Coherent Light Source (LCLS) using AT_1R micro-crystals (average size 10×2×2 μm^3) grown in syringes (Figure S1B,C). A total of 2,764,739 patterns were collected by using ~65 μL of crystal-loaded LCP, corresponding to ~0.35 mg of protein. Of these frames, 457,275 were identified as crystal hits, corresponding to a hit rate of 17%. Of these crystal hits, 73,130 frames (16%) were successfully indexed and integrated by CrystFEL (White et al., 2012) to 2.9 Å resolution (Table S1 and Figure S1D–F). The structure of the AT_1R-ZD7155 complex was refined to R_{work}/R_{free} of 22.8%/27.4%. The final structure includes 289 out of 359 residues in the full-length human AT_1R (Figure 1A), and it has well-defined densities for most AT_1R residues and for the ligand ZD7155.

Overall architecture of AT_1R

AT_1R, being the angiotensin II octapeptide receptor, shares some sequence similarity with other peptide receptors of class A GPCRs, structures of which are known (sequence alignment is shown in Figure S2), with the closest homology to the chemokine receptors (e.g. 36% sequence identity with CXCR4) and opioid receptors (e.g. 33% sequence identity with κ-OR) (Wu et al., 2010; Wu et al., 2012). AT_1R exhibits the canonical seven transmembrane α-helical (7TM) architecture, with an extracellular N-terminus, three intracellular loops (ICL1-3), three extracellular loops (ECL1-3), an amphipathic helix VIII and an intracellular C-terminus (Figure 2A). The overall fold of the angiotensin receptor AT_1R is most similar to the chemokine and opioid receptors (Figure 2B), with the lowest root mean square deviation for 80% of AT_1R α-carbon atoms ($RSMD_{Cα}$) of about 1.8 Å to

the nociceptin/orphanin FQ peptide receptor (NOP) (Thompson et al., 2012). Despite the overall similarity, a number of structural differences in the transmembrane bundle were observed between AT_1R and other peptide GPCRs (Figures 2C,D). For example, the tilts and extensions of the extracellular ends of helices I, V, VI and VII are substantially different among these peptide receptors, while at the intracellular side, helices IV and V adopt the most diverse conformations. The conformations of helices II and III, however, are nearly identical for all these peptide receptors.

The extracellular part of AT_1R consists of the N-terminal segment, ECL1 (Glu91-Phe96) linking helices II and III, ECL2 (His166 to Ile191) linking helices IV and V, and ECL3 (Ile270 to Cys274) linking helices VI and VII (Figure 1A). Two disulfide bonds help to shape the extracellular side of AT_1R, with Cys18-Cys274 connecting the N-terminus and ECL3, and Cys101-Cys180 connecting helix III and ECL2, similar to the chemokine receptors CXCR4 and CCR5 (Wu et al., 2010; Tan et al., 2013). Besides engaging in the conserved disulfide bonding, ECL2 of AT_1R exhibits a β-hairpin secondary structure, a common motif among peptide GPCRs (Figure 2E). Intriguingly, ECL2 of AT_1R was found to serve as an epitope for the harmful agonistic autoantibodies in preeclampsia and malignant hypertension (Unal et al., 2012; Xia and Kellems, 2013).

The intracellular portion of AT_1R contains ICL1 (Lys58 to Val62) linking helices I and II, ICL2 (Val131 to Arg137) linking helices III and IV, ICL3 (Leu222 to Asn235) linking helices V and VI, and the C-terminal helix VIII. As in many other class A GPCRs, the conserved D(E)RY motif in helix III and the NPxxY motif in helix VII of AT_1R, both at the intracellular ends of transmembrane domain, were proposed to participate in receptor activation (Oliveira et al., 2007). However, the “ionic lock” salt bridge interaction between $Arg^{3.50}$ (superscript indicates residue number as per the Ballesteros-Weinstein, 1995 (B&W) nomenclature) of the D(E)RY motif and $Asp/Glu^{6.30}$ at the cytoplasmic end of helix VI is not possible in AT_1R, because the human AT_1R lacks an acidic residue at the position 6.30.

The C-terminal helix VIII of AT_1R was shown to bind the calcium-regulated effector protein, calmodulin (Thomas et al., 1999). Integrity of this region is also important for receptor internalization and coupling to G protein activation and signaling (Thomas et al., 1995; Sano et al., 1997). In most previously solved GPCR structures, helix VIII runs parallel to the membrane bilayer, however, in AT_1R it angles away from the membrane, resembling the orientation of this helix in CCR5 (Figure 2F). Experimentally, the secondary structure of AT_1R helix VIII was observed to be sensitive to hydrophobic environment, thereby associating with the cytoplasmic side of the cell membrane via a high-affinity, anionic phospholipid-specific tethering that serves to increase the amphipathic helicity of this region (Mozsolits et al., 2002). As a separate peptide, helix VIII of AT_1R showed a higher affinity for lipid membranes that contained negatively charged phospholipids, rather than zwitterionic phospholipids (Kamimori et al., 2005). A high concentration of positively charged residues (306-KKFKR-312) in helix VIII of AT_1R possibly defines its orientation and explains its sensitivity to the negatively charged lipids. Moreover, in AT_1R there is no putative palmitoylation site that is present in many GPCRs in this region, anchoring helix VIII to the lipid membrane.

ZD7155 interactions in AT_1R ligand-binding pocket

Small molecule antagonist ZD7155 was modeled into the prominent and well-defined electron density inside the ligand-binding pocket of AT_1R (Figure 3A,B), interacting with residues mainly from helices I, II, III, and VII, as well as ECL2. Side chains of $Arg167^{ECL2}$ and $Tyr35^{1.39}$ were found to form ionic and hydrogen bond interactions with ZD7155. The positively charged guanidine group of $Arg167^{ECL2}$ forms an extensive interaction network with the acidic tetrazole and the naphthyridin-2-one moieties of ZD7155. Leveraging this information in mutagenesis studies, we found that mutation of $Arg167^{ECL2}$ to alanine abolished both the peptide and non-peptide ligands binding to AT_1R (Table S2). However, the $Arg167^{ECL2}$Lys mutant showed only 2–3 fold reduced binding affinities for ZD7155, which can be explained by the ability of lysine in this position to engage in salt bridge and hydrogen bond interactions similar to $Arg167^{ECL2}$, although likely with less optimal interaction geometry. The tetrazole moiety, or other acidic isostere in the ortho position of the biphenyl group comprises the most common scaffold among ARBs, and $Arg167^{ECL2}$ is a unique residue of AT_1R compared to other structurally similar peptide GPCRs (Figure S2). This observation suggests that $Arg167^{ECL2}$ may play an essential role in determining AT_1R ligand-binding affinity and selectivity. An additional hydrogen bond forms between $Tyr35^{1.39}$ and the naphthyridin-2-one moiety of ZD7155. Our data showed that the $Tyr35^{1.39}$Ala mutant abolishes the binding capabilities of both peptide and non-peptide ligands with AT_1R (Table S2). $Tyr^{1.39}$ is a well conserved residue in the angiotensin, chemokine, and opioid receptors (Figure S2). In the CCR5 structure, for example, $Tyr37^{1.39}$ interacts with its ligand maraviroc (Tan et al., 2013).

The ZD7155 binding site in AT_1R partially overlaps with known ligand binding sites in the chemokine and opioid receptors (Figures 2G,H). Intriguingly, some of the residues that comprise the ligand-binding pockets, including $Ile^{1.35}$, $Phe^{2.53}$, $Trp^{2.60}$, and $Tyr^{7.43}$, can be found among these structurally similar peptide GPCRs (Figure S2). Residues $Phe77^{2.53}$ and $Trp84^{2.60}$ from helix II of AT_1R are conserved in the chemokine receptors CXCR4 and CCR5 (Wu et al., 2010; Tan et al., 2013). Particularly, $Trp84^{2.60}$ of AT_1R forms π-π interaction with the naphthyridin-2-one moiety of ZD7155, and mutation of $Trp84^{2.60}$ to alanine abolished both the peptide and non-peptide ligands binding to AT_1R (Figure 3C and Table S2). Residues $Ile31^{1.35}$ and $Tyr292^{7.43}$ from helices I and VII of AT_1R are conserved in the opioid receptors κ-OR, δ-OR, and NOP. Additionally, residues $Val108^{3.32}$ and $Leu112^{3.36}$, which hydrophobically interact with ZD7155 in the AT_1R ligand-binding pocket, are replaced by $Tyr108^{3.32}$ and $Phe112^{3.36}$ in CCR5 and form hydrophobic interactions with its ligand maraviroc. In contrast, the position 3.32 in the aminergic and opioid receptors is occupied by a conserved aspartic acid that engages in a salt bridge interaction with ligands. Most of the other contacts for ZD7155 binding to AT_1R, however, are mediated by non-conserved residues, including $Tyr87^{2.63}$, $Thr88^{2.64}$, $Ser105^{3.29}$, $Ser109^{3.33}$, $Ala163^{4.60}$, $Phe182^{ECL2}$, $Pro285^{7.36}$, and $Ile288^{7.39}$ (Figures 3B,C and Figure S2). These residues along with $Arg167^{ECL2}$ therefore define the unique shape of the AT_1R ligand-binding pocket and explain the lack of cross-reactivity between ligands binding to AT_1R and other peptide receptors.

Binding modes of different ARBs toward AT_1R

To analyze the common and diverse features of the binding modes for different ARBs in AT_1R, we performed energy-based docking simulations of the clinically used anti-hypertensive ARBs using the AT_1R structure. The docking results show robust positioning of these compounds in the AT_1R ligand-binding pocket (Figure 4 and Table S3). Although the nature of the interactions with AT_1R is different for each ARB given their distinct chemical structures, most of these compounds are bound in similar orientations and engage in interactions with the three residues critical for ZD7155 binding, Arg167^{ECL2}, Trp84$^{2.60}$, and Tyr35$^{1.39}$ (Figure 5). Residues Phe77$^{2.53}$, Tyr87$^{2.63}$, Ser105$^{3.29}$, Val108$^{3.32}$, Ser109$^{3.33}$, Leu112$^{3.36}$, Ala163$^{4.60}$, Phe182^{ECL2}, Ile288$^{7.39}$, and Tyr292$^{7.43}$ also contribute to the receptor-ligand interactions and shape the ligand-binding pocket. For example, one of the common features among these ARBs is a short alkyl tail with two-four carbons extending into a narrow hydrophobic pocket formed by Tyr35$^{1.39}$, Phe77$^{2.53}$, Val108$^{3.32}$, Ile288$^{7.39}$, and Tyr292$^{7.43}$ (Figure 5).

Losartan is the first clinically used ARB for the treatment of hypertension. It is, however, a surmountable antagonist with lower binding affinity to AT_1R compared to the later developed ARBs (Miura et al., 2011). Docking results suggest that Arg167^{ECL2} forms a salt bridge only with the tetrazole moiety of losartan but lacks polar interactions with other groups (Figure 4 and Table S3). Although the derived imidazole moiety of losartan can also contribute to polar interactions via methanol hydrogen bond to Cys180^{ECL2} main chain or via nitrogen interaction with Tyr35$^{1.39}$, distances and angles for hydrogen bonding are suboptimal; this may explain the lower binding affinity and surmountable property of losartan at AT_1R. An active metabolite of losartan, EXP3174, is predicted to bind in a similar pose as losartan, but instead of interaction with Cys180^{ECL2}, its carboxyl group could engage in a second salt bridge interaction with Arg167^{ECL2}, similarly to ZD7155 (Table S3). In contrast, candesartan is an insurmountable inverse agonist with a slow dissociation rate from AT_1R (Takezako et al., 2004). The docking results indicate that besides interacting with the tetrazole moiety of candesartan, Arg167^{ECL2} forms two salt bridges to the carboxylic group of the benzimidazole moiety (Figure 4 and Table S3). Moreover, Lys199$^{5.42}$ is predicted to form an additional salt bridge with the tetrazole moiety, which can further stabilize candesartan binding. Telmisartan lacks the conserved tetrazole moiety among ARBs. Instead, the carboxylic group of telmisartan is predicted to form salt bridges with both Arg167^{ECL2} and Lys199$^{5.42}$ (Figure 4 and Table S3). Moreover, unlike other ARBs studied here, two consecutive benzimidazole moieties of telmisartan extend to Tyr92^{ECL1}, making additional hydrophobic and π-π contacts, which are likely to contribute to its high potency (Balakumar et al., 2012). This prediction was confirmed by our mutagenesis data, which showed a dramatic decrease in affinity of telmisartan to the Tyr92^{ECL1}Ala mutant (Figure S3A). Eprosartan is the most unique among the ARBs studied here, lacking both the tetrazole group and one of the two benzene rings of the biphenyl scaffold. As our docking results suggest, eprosartan uses its two carboxyl groups to form salt bridges with Arg167^{ECL2} (Figure 4 and Table S3). Additionally, the specific thiophen moiety of eprosartan forms hydrophobic interactions with Pro285$^{7.36}$ and Ile288$^{7.39}$ and reaches toward Met284$^{7.35}$. Mutation of Met284$^{7.35}$ to alanine produced minimal effect, slightly increasing the affinity for eprosartan binding, in agreement with predicted

interactions of this ligand with only mainchain and C_β atoms of Met284$^{7.35}$ (Figure S3B). On the other hand, mutations Pro285$^{7.36}$Ala and Ile288$^{7.39}$Ala induced a strong decrease in the binding affinity of eprosartan (Figure S3C,D), highlighting essential role of these residues in eprosartan binding. Finally, both our crystal structure and docking results suggest that Lys199$^{5.42}$ retains some conformational heterogeneity in AT_1R. Docking with the flexible side chain of Lys199$^{5.42}$ indicates that the amino group of this residue can reach the acidic moieties of ARBs by forming salt bridges (as interacting with candesartan and telmisartan) or water-mediated interactions, which may explain the reduced ligand-binding capabilities of Lys199$^{5.42}$ mutants (Table S2).

Mechanism of AT_1R modulation

Based on previous observations that mutations of either Asn111$^{3.35}$ or Asn295$^{7.46}$ induce constitutive activation of the receptor, it was proposed that the inactive conformation of AT_1R is stabilized by interactions between Asn111$^{3.35}$ and Asn295$^{7.46}$. Further, it was suggested that binding of AngII to the wild-type (WT) receptor disrupts the hydrogen bonds between Asn111$^{3.35}$ and Asn295$^{7.46}$, thus allowing Asn295$^{7.46}$ to interact with the conserved Asp74$^{2.50}$ (Balakumar and Jagadeesh, 2014; Unal and Karnik, 2014). Indeed, two intramolecular hydrogen bonds are observed between Asn111$^{3.35}$ and Asn295$^{7.46}$ in the AT_1R-ZD7155 structure (Figure 6A). Of particular interest, Asp74$^{2.50}$, Asn111$^{3.35}$, and Asn295$^{7.46}$, together with two other residues, Trp253$^{6.48}$ from the WxP motif and Asn298$^{7.49}$ from the NPxxY motif, belong to the putative sodium pocket of AT_1R (Katritch et al, 2014) as revealed by superposition with the sodium site in the high-resolution structure of δ-OR (Figure 6B) (Fenalti et al., 2014). All residues lining this pocket in AT_1R are conserved exactly as in δ-OR, except for Asn295$^{7.46}$ (Ser in δ-OR), which is observed at this position in a GPCR structure for the first time; therefore, its presence and the strong hydrogen bond interactions with Asn111$^{3.35}$ may impact the sodium binding and functional properties of AT_1R. Moreover, the neighboring residue Phe77$^{2.53}$ from the ligand-binding pocket of AT_1R was also found to be critical for the inter-helical interactions required for AT_1R activation (Miura et al., 2003). Combination of Phe77$^{2.53}$Ala and Asn111$^{3.35}$Gly mutations resulted in an almost fully active receptor (Miura et al., 2008). Thus, multiple structural and functional data suggest that the hydrogen bond network around Asn111$^{3.35}$ and Asn295$^{7.46}$ as revealed in the current structure may play an essential role in AT_1R activation, probably by relaying the conformational changes in the ligand-binding pocket to the cytoplasmic domain coupling to the downstream signaling, although further structural, functional, and biophysical studies are required to fully understand the mechanism of AT_1R modulation.

DISCUSSION

The angiotensin receptor AT_1R is a therapeutic target of outstanding interest due to its important roles in cardiovascular pathophysiology. Several AT_1R blockers have been developed and clinically used as anti-hypertensive drugs. Although extensive efforts were taken to delineate the pharmacophores of AT_1R ligands, structure-based drug design was still hindered by the lack of structural information. By using an XFEL, we successfully determined the crystal structure of the human AT_1R in complex with its antagonist ZD7155.

Compared to the traditional X-ray crystallography with cryo-cooled crystals, the LCP-SFX method yields the room-temperature structure of the AT_1R-ZD7155 complex, which is likely to represent more accurately the receptor conformations and dynamics in the native cellular environment. The AT_1R-ZD7155 complex structure reveals a variety of key features of AT_1R shared with other GPCR family members, as well as many novel and unique structural characteristics of the angiotensin receptor. Unexpectedly, three AT_1R residues, which have not been previously implicated in binding small molecule ligands, were found to form critical interactions with ZD7155; $Arg167^{ECL2}$ and $Tyr35^{1.39}$ are engaged in ionic and hydrogen bonds, while $Trp84^{2.60}$ forms extensive π-π interactions with the ligand. The antagonist-bound AT_1R structure was used further for docking of several anti-hypertensive ARBs into the AT_1R ligand-binding pocket, elucidating the structural basis for AT_1R modulation by drugs. Our extensive mutagenesis experiments revealed that residues $Tyr35^{1.39}$, $Trp84^{2.60}$, $Arg167^{ECL2}$, and $Lys199^{5.42}$ are critical for both peptide ([Sar^1, Ile^8]-AngII) and non-peptide (candesartan) binding. Residues $Phe182^{ECL2}$ and $Ile288^{7.39}$ discriminate between the peptide and non-peptide ligand (these mutants do not bind [Sar^1, Ile^8]-AngII but bind candesartan). Mutations of $Ser109^{3.33}$ and $Tyr292^{7.43}$ slightly affected non-peptide (candesartan) binding but not peptide binding (Table S2).

Among the naturally occurring amino acid variations in AT_1R, reported in Uniprot (http://www.uniprot.org/uniprot/P30556), $Ala163^{4.60}$Thr, $Thr282^{7.33}$Met, and $Cys289^{7.40}$Trp are located near the binding pocket for ARBs. These variants may directly alter binding of ARBs and therefore modify the anti-hypertensive response to treatment with different ARBs in individuals carrying these variations. In contrast, $Leu48^{1.52}$Val, $Leu222^{ICL3}$Val, and $Ala244^{6.39}$Ser, which are located closer to intracellular ends of helices, may indirectly influence binding of ARBs or signaling by AT_1R. Finally, Thr336Pro and Pro341His are located in the C-terminal tail that was not included in the crystalized construct. These residues, however, are known to affect GPCR kinase-dependent phosphorylation, an event that is necessary for β-arrestin recruitment to AT_1R.

Of particular interest, the atomic details of ECL2 and the extracellular ligand-binding region, revealed in the current structure, are expected to guide design of two different types of therapeutic agents targeting AT_1R, the anti-hypertensive ARBs extensively interacting with $Arg167^{ECL2}$ on the ligand-binding pocket side of ECL2, and the peptide-mimicking antigens against autoantibodies, which bind to the extracellular side of ECL2 in patients with autoimmune disorders, such as preeclampsia and malignant hypertension (Zhou et al, 2008; Fu et al, 2000). Therefore, our results provide long anticipated insights into the AT_1R structure-function relationship and pharmacological properties, and demonstrate the potential for using the LCP-SFX method at XFEL sources to accelerate structural studies of challenging targets.

EXPERIMENTAL PROCEDURES

Protein engineering for structural studies

The sequence of the human AT_1R gene was optimized for insect cells expression and synthesized by GenScript. A thermostabilized apocytochrome b_{562}RIL (BRIL) from *E. coli* (M7W, H102I, R106L) was fused to the N-terminus of the human AT_1R, using overlapping

PCR. The construct has truncations of the AT_1R residues 1, 7–16, and 320–359. The resulting BRIL-AT_1R chimera sequence was subcloned into a modified pFastBac1 vector (Invitrogen), which contains a haemagglutinin (HA) signal sequence, a FLAG tag and 10×His tag, followed by a tobacco etch virus (TEV) protease cleavage site, before the N-terminus of the chimera sequence.

Protein expression and purification

BRIL-AT_1R construct was expressed in *Spodoptera frugiperda* (Sf9) insect cells using the Bac-to-Bac baculovirus expression system (Invitrogen). Cells with a density of 2–3×10^6 cells per ml were infected with baculovirus at 27 °C, and harvested at 48 hours after infection.

BRIL-AT_1R in complex with ZD7155 (Tocris Bioscience) was solubilized from isolated membranes using 1% (w/v) n-dodecyl-beta-D-maltopyranoside (DDM, Anatrace) and 0.2% (w/v) cholesterol hemisuccinate (CHS, Sigma-Aldrich). After purification by metal affinity chromatography BRIL-AT_1R/ZD7155 complex was desalted to remove imidazole using PD MiniTrap G-25 column (GE Healthcare), and then treated overnight with His-tagged TEV protease to cleave the N-terminal FLAG/His tags from the protein. The cleaved FLAG/His tags and TEV protease were removed by TALON IMAC resin. The protein was not treated with PNGase F and therefore remained fully glycosylated. Finally, the purified protein was concentrated to 30 mg/ml with a 100 kDa cutoff concentrator (Vivaspin) and used in crystallization trials. The protein yield and monodispersity were tested by analytical size exclusion chromatography (aSEC).

Lipidic cubic phase crystallization

BRIL-AT_1R in complex with ZD7155 was crystallized in LCP composed of monoolein supplemented with 10% cholesterol (Caffrey and Cherezov, 2009). LCP crystallization trials were performed using an NT8-LCP crystallization robot (Formulatrix). 96-well glass sandwich plates (Marienfeld) were incubated and imaged at 20 °C using an automatic incubator/imager (RockImager 1000, Formulatrix). The crystals grew in the condition of 100 mM sodium citrate, pH 5.0–6.0, 300–600 mM $NH_4H_2PO_4$, 20–30% (v/v) PEG400 and 2–8% (v/v) DMSO. The crystals were harvested using micromounts (MiTeGen) and flash-frozen in liquid nitrogen for data collection at a synchrotron source. These crystals diffracted only to about 4 Å resolution, even after extensive optimization of crystallization conditions.

Microcrystals for SFX data collection were prepared in gas-tight syringes (Hamilton) as described (Liu et al., 2014b), using 100 mM sodium citrate, pH 5.0, 450 mM $NH_4H_2PO_4$, 28% (v/v) PEG400 and 4% (v/v) DMSO as a precipitant. Before loading microcrystals in the LCP injector the excess precipitant was removed, and 7.9 MAG was added and mixed with LCP, to absorb the residual precipitant solution and prevent formation of a crystalline phase due to a rapid evaporative cooling when injecting LCP into vacuum (Weierstall et al., 2014).

X-ray free electron laser data collection

Data collection was performed at the Coherent X-ray Imaging (CXI) end station of the Linac Coherent Light Source (LCLS), SLAC National Accelerator Laboratory, using XFEL pulses

of 36 fs duration focused to a size of 1.5×1.5 μm^2 by Kirkpatrick-Baez mirrors. A photon energy of 7.9 keV, an average pulse energy of 2.7 mJ and a transmission level of 16% resulted in a maximum dose of 75 MGy at the sample.

Microcrystals dispersed in LCP were delivered into the interaction region using an LCP injector (Weierstall et al., 2014) with a 50 μm diameter nozzle at a flow rate of 170 nl per minute. Diffraction patterns were collected on a Cornell-SLAC Pixel array detector (CSPAD - version 1.5) (Hart et al., 2012) at a rate of 120 Hz.

With a total sample volume of 65 μl, a total of 2,764,739 diffraction frames were collected within 6.4 hours. Initial frames were corrected and filtered using the software package Cheetah (Barty et al., 2014). A crystal 'hit' was defined as an image containing a minimum of 15 diffraction peaks with a signal to noise ratio above 4. A total of 457,275 positive 'hits' were further processed using the CrystFEL software suite (version 0.5.3) (White et al., 2012). The detector geometry was refined using an automated algorithm designed to match found and predicted peaks to sub-pixel accuracy. By further refinement of parameters (peak detection, prediction and integration), a total of 73,130 images were indexed, integrated and merged into a final dataset. To reduce noise and outliers and thus improve data quality we have applied two data rejection criteria: 1) per pattern resolution cutoff, and 2) rejection of patterns based on a Pearson correlation coefficient threshold, as described in the Extended Experimental Procedures. A resolution cutoff was estimated to be 2.9 Å using a combination of *CC** (Karplus and Diederichs, 2012) and other parameters (Figure S1D–F). The final dataset had overall R_{split}=9.8%, and *CC**=0.872 in the highest resolution shell.

Structure determination

The structure was solved by molecular replacement with Phaser (McCoy et al., 2007) using an automated script described in the Extended Experimental Procedures.

Refinement and model completion were performed by repetitive cycling between Refmac5 (Murshudov et al., 1997) and autoBUSTER (Bricogne et al., 2009), followed by manual examination and rebuilding of the refined coordinates in Coot (Emsley et al., 2010). Data collection and refinement statistics are shown in Table S1.

Docking of ARBs into AT_1R ligand-binding pocket

Representative ARBs were docked into the AT_1R crystal structure using an energy-based docking protocol implemented in ICM molecular modeling software suite (Molsoft). Molecular models of compounds were generated from two-dimensional representations and their 3D geometry was optimized using MMFF-94 force field (Halgren, 1995). Molecular docking employed biased probability Monte Carlo (BPMC) optimization of the ligand internal coordinates in the grid potentials of the receptor (Totrov and Abagyan, 1997). To assure convergence of the docking procedure, at least five independent docking runs were performed for each ligand starting from a random conformation;. The results of individual docking runs for each ligand were considered consistent if at least three of the five docking runs produced similar ligand conformations (RMSD < 2.0 Å) and Binding Score < −20.0 kJ/

mol. The unbiased docking procedure did not use distance restraints or any other *a priori* derived information for the ligand-receptor interactions.

Ligand binding assays

Ligand binding was analyzed using total membranes prepared from COS-1 cells transiently expressing HA-AT_1R (wild type), ΔBRIL-AT_1R (crystallized construct without BRIL), and BRIL-AT_1R (crystallized construct) constructs. Single mutants were constructed by a PCR-based site-directed mutagenesis strategy as previously described (Unal et al., 2010). Protein concentration was determined by Bio-Rad Protein Assay (Bio-Rad). For both saturation and competition binding assays, 10 μg of homogenous cell membrane was used per well.

Saturation binding assays with ^{3}H-candesartan were performed under equilibrium conditions, with ^{3}H-candesartan (Amersham Pharmacia Biotech) concentrations ranging between 0.125 and 12 nM (specific activity, 16 Ci/mmol) as duplicates in 96-well plates for 1h at room temperature. Nonspecific binding was measured in the presence of 10 μM candesartan (gift from AstraZeneca). The binding kinetics was analyzed by nonlinear curve-fitting program GraphPad Prism 5, which yields the mean ± S.D. for the K_d and B_{max} values.

Competition binding assays were performed under equilibrium conditions, with 2 nM ^{3}H-candesartan and various concentrations of the ZD7155 ranging between 0.04 and 1000 nM. The binding kinetics was analyzed by nonlinear curve-fitting program GraphPad Prism 5, which yields the mean ± S.D. for the IC_{50} values.

Signaling assays in whole cells

Calcium levels inside COS-1 cells transiently expressing different AT_1R constructs were measured using a Fluorescent Imaging Plate Reader (FLIPR®) Calcium 5 assay kit (Molecular Devices). For the antagonist dose-response, the cells were first treated with different concentrations of ZD7155 for 1h followed by stimulation with 100 nM AngII. The EC50 values for AngII dose response were 0.2, 2, and 12 nM for HA-AT_1R, ΔBRIL-AT_1R, and BRIL-AT_1R, respectively. The IC50 values for ZD7155 to inhibit AngII response were between 3 to 4 nM for all constructs. The curves from a representative experiment wherein measurements are made in triplicate are shown as mean ± SEM. Additional information is available in the Extended Experimental Procedures.

Supplementary Material

Refer to Web version on PubMed Central for supplementary material.

ACKNOWLEDGMENTS

This work was supported in parts by the National Institutes of Health (NIH) grants R01 GM108635 (V.C.); U54 GM094618 (target GPCR-11) (V.K., V.C., R.C.S.); P41 GM103393 (S.B.); R01 HL57470 (S.S.K.); R01 HL115964 (S.S.K.); U54 GM094599 (P.F.); R01 GM095583 (P.F.); U54 GM094586 (Q.X.); National Research Service award HL007914 (H.U.). Further support was provided by the National Science Foundation (NSF) BioXFEL Science and Technology center grant 1231306 (P.F., U.W, G.N.); the Helmholtz Gemeinschaft, the DFG Cluster of Excellence ‘Center for Ultrafast Imaging’; the BMBF project FKZ 05K12CH1 (C.G., O.M.Y., T.A.W.); the PIER Helmholtz Graduate School and the Helmholtz Association (C.G.); and the Chinese 1000 Talent Program

(R.C.S.). Parts of this research were carried out at the LCLS, a National User Facility operated by Stanford University on behalf of the U.S. Department of Energy, Office of Basic Energy Sciences, and at the GM/CA CAT of the Argonne Photon Source, Argonne National Laboratory. We thank J. Velasquez for help with molecular biology, T. Trinh and M. Chu for help with baculovirus expression, M. Metz, D. Oberthuer, A. Barty, S. Basu and R. Fromme for help with the XFEL data collection and analysis, and R. Miller, K. Kadyshevskaya and A. Walker for assistance with manuscript preparation. We are grateful to J. Spence and H. Chapman for their encouragement and support.

REFERENCES

Akazawa H, Yano M, Yabumoto C, Kudo-Sakamoto Y, Komuro I. Angiotensin II type 1 and type 2 receptor-induced cell signaling. Curr Pharm Des. 2013; 19:2988–2995. [PubMed: 23176210]

Balakumar P, Bishnoi HK, Mahadevan N. Telmisartan in the management of diabetic nephropathy: a contemporary view. Curr Diabetes Rev. 2012; 8:183–190. [PubMed: 22429010]

Balakumar P, Jagadeesh G. Structural determinants for binding, activation and functional selectivity of the AT1 receptor. J Mol Endocrinol. 2014; 53:R71–R92. [PubMed: 25013233]

Ballesteros JA, Weinstein H. Integrated methods for the construction of three dimensional models and computational probing of structure–function relations in G-protein coupled receptors. Methods Neurosci. 1995; 25:366–428.

Barty A, Kirian RA, Maia FR, Hantke M, Yoon CH, White TA, Chapman H. Cheetah: software for high-throughput reduction and analysis of serial femtosecond X-ray diffraction data. J Appl Crystallogr. 2014; 47:1118–1131. [PubMed: 24904246]

Bricogne, G.; Blanc, E.; Brandl, M.; Flensburg, C.; Keller, P.; Paciorek, W.; Roversi, P.; Sharff, A.; Smart, OS.; Vonrhein, C., et al. Buster version 2.8.0. Cambridge, United Kingdom: Global Phasing Ltd; 2009.

Burnier M, Brunner HR. Angiotensin II receptor antagonists. Lancet. 2000; 355:637–645. [PubMed: 10696996]

Caffrey M, Cherezov V. Crystallizing membrane proteins using lipidic mesophases. Nat Protoc. 2009; 4:706–731. [PubMed: 19390528]

Chun E, Thompson AA, Liu W, Roth CB, Griffith MT, Katritch V, Kunken J, Xu F, Cherezov V, Hanson MA, et al. Fusion partner toolchest for the stabilization and crystallization of G protein-coupled receptors. Structure. 2012; 20:967–976. [PubMed: 22681902]

de Gasparo M, Catt KJ, Inagami T, Wright JW, Unger T. International union of pharmacology. XXIII. The angiotensin II receptors. Pharmacol Rev. 2000; 52:415–472. [PubMed: 10977869]

Emsley P, Lohkamp B, Scott WG, Cowtan K. Features and development of Coot. Acta Crystallogr Section D, Biol Crystallogr. 2010; 66:486–501. [PubMed: 20383002]

Fenalti G, Giguere PM, Katritch V, Huang XP, Thompson AA, Cherezov V, Roth BL, Stevens RC. Molecular control of delta-opioid receptor signalling. Nature. 2014; 506:191–196. [PubMed: 24413399]

Fu ML, Herlitz H, Schulze W, Wallukat G, Micke P, Eftekhari P, Sjogren KG, Hjalmarson A, Muller-Esterl W, Hoebeke J. Autoantibodies against the angiotensin receptor (AT1) in patients with hypertension. J Hypertens. 2000; 18:945–953. [PubMed: 10930193]

Halgren T. Merck molecular force field I–V. J Comp Chem. 1995; 17:490–641.

Hart, P.; Boutet, S.; Carini, G.; Dragone, A.; Duda, B.; Freytag, D.; Haller, G.; Herbst, R.; Herrmann, S.; Kenney, C., et al. The Cornell-SLAC Pixel Array Detector at LCLS; Nuclear Science Symposium, Medical Imaging Conference; 2012.

Imaizumi S, Miura S, Yahiro E, Uehara Y, Komuro I, Saku K. Class- and molecule-specific differential effects of angiotensin II type 1 receptor blockers. Curr Pharm Des. 2013; 19:3002–3008. [PubMed: 23176212]

Junggren IL, Zhao X, Sun X, Hedner T. Comparative cardiovascular effects of the angiotensin II type 1 receptor antagonists ZD 7155 and losartan in the rat. J Pharm Pharmacol. 1996; 48:829–833. [PubMed: 8887734]

Kamimori H, Unabia S, Thomas WG, Aguilar MI. Evaluation of the membrane-binding properties of the proximal region of the angiotensin II receptor (AT1A) carboxyl terminus by surface plasmon resonance. Anal Sci. 2005; 21:171–174. [PubMed: 15732479]

Karplus PA, Diederichs K. Linking crystallographic model and data quality. Science. 2012; 336:1030–1033. [PubMed: 22628654]

Katritch V, Fenalti G, Abola EE, Roth BL, Cherezov V, Stevens RC. Allosteric sodium in class A GPCR signaling. Trends Biochem Sci. 2014; 39:233–244. [PubMed: 24767681]

Keane MG, Pyeritz RE. Medical management of Marfan syndrome. Circulation. 2008; 117:2802–2813. [PubMed: 18506019]

Liu W, Wacker D, Wang C, Abola E, Cherezov V. Femtosecond crystallography of membrane proteins in the lipidic cubic phase. Phil Trans R Soc B. 2014a; 369:20130314. [PubMed: 24914147]

Liu W, Ishchenko A, Cherezov V. Preparation of microcrystals in lipidic cubic phase for serial femtosecond crystallography. Nat Protoc. 2014b; 9:2123–2134. [PubMed: 25122522]

Liu W, Wacker D, Gati C, Han GW, James D, Wang D, Nelson G, Weierstall U, Katritch V, Barty A, et al. Serial femtosecond crystallography of G protein-coupled receptors. Science. 2013; 342:1521–1524. [PubMed: 24357322]

Lomize MA, Pogozheva ID, Joo H, Mosberg HI, Lomize AL. OPM database and PPM web server: resources for positioning of proteins in membranes. Nucleic Acids Res. 2012; 40:D370–D376. [PubMed: 21890895]

Ma TK, Kam KK, Yan BP, Lam YY. Renin-angiotensin-aldosterone system blockade for cardiovascular diseases: current status. Br J Pharmacol. 2010; 160:1273–1292. [PubMed: 20590619]

McCoy AJ, Grosse-Kunstleve RW, Adams PD, Winn MD, Storoni LC, Read RJ. Phaser crystallographic software. J Appl Crystallogr. 2007; 40:658–674. [PubMed: 19461840]

Miura S, Karnik SS, Saku K. Review: angiotensin II type 1 receptor blockers: class effects versus molecular effects. J Renin Angiotensin Aldosterone Syst. 2011; 12:1–7. [PubMed: 20603272]

Miura S, Kiya Y, Kanazawa T, Imaizumi S, Fujino M, Matsuo Y, Karnik SS, Saku K. Differential bonding interactions of inverse agonists of angiotensin II type 1 receptor in stabilizing the inactive state. Mol Endocrinol. 2008; 22:139–146. [PubMed: 17901125]

Miura S, Nakao N, Hanzawa H, Matsuo Y, Saku K, Karnik SS. Reassessment of the unique mode of binding between angiotensin II type 1 receptor and their blockers. PloS One. 2013a; 8:e79914. [PubMed: 24260317]

Miura S, Okabe A, Matsuo Y, Karnik SS, Saku K. Unique binding behavior of the recently approved angiotensin II receptor blocker azilsartan compared with that of candesartan. Hypertens Res. 2013b; 36:134–139. [PubMed: 23034464]

Miura S, Zhang J, Boros J, Karnik SS. TM2-TM7 interaction in coupling movement of transmembrane helices to activation of the angiotensin II type-1 receptor. J Biol Chem. 2003; 278:3720–3725. [PubMed: 12446719]

Mozsolits H, Unabia S, Ahmad A, Morton CJ, Thomas WG, Aguilar MI. Electrostatic and hydrophobic forces tether the proximal region of the angiotensin II receptor (AT1A) carboxyl terminus to anionic lipids. Biochemistry. 2002; 41:7830–7840. [PubMed: 12056915]

Murshudov GN, Vagin AA, Dodson EJ. Refinement of macromolecular structures by the maximum-likelihood method. Acta Crystallogr Section D, Biol Crystallogr. 1997; 53:240–255. [PubMed: 15299926]

Oliveira L, Costa-Neto CM, Nakaie CR, Schreier S, Shimuta SI, Paiva AC. The angiotensin II AT1 receptor structure-activity correlations in the light of rhodopsin structure. Physiol Rev. 2007; 87:565–592. [PubMed: 17429042]

Ramanath VS, Oh JK, Sundt TM 3rd, Eagle KA. Acute aortic syndromes and thoracic aortic aneurysm. Mayo Clinic proceedings. 2009; 84:465–481. [PubMed: 19411444]

Ramchandran R, Takezako T, Saad Y, Stull L, Fink B, Yamada H, Dikalov S, Harrison DG, Moravec C, Karnik SS. Angiotensinergic stimulation of vascular endothelium in mice causes hypotension, bradycardia, and attenuated angiotensin response. Proc Natl Acad Sci USA. 2006; 103:19087–19092. [PubMed: 17148616]

Sano T, Ohyama K, Yamano Y, Nakagomi Y, Nakazawa S, Kikyo M, Shirai H, Blank JS, Exton JH, Inagami T. A domain for G protein coupling in carboxyl-terminal tail of rat angiotensin II receptor type 1A. J Biol Chem. 1997; 272:23631–23636. [PubMed: 9295303]

Shenoy SK, Lefkowitz RJ. Angiotensin II-stimulated signaling through G proteins and beta-arrestin. Sci STKE. 2005; 2005:cm14. [PubMed: 16304060]

Takezako T, Gogonea C, Saad Y, Noda K, Karnik SS. "Network leaning" as a mechanism of insurmountable antagonism of the angiotensin II type 1 receptor by non-peptide antagonists. J Biol Chem. 2004; 279:15248–15257. [PubMed: 14754891]

Tan Q, Zhu Y, Li J, Chen Z, Han GW, Kufareva I, Li T, Ma L, Fenalti G, Li J, et al. Structure of the CCR5 chemokine receptor-HIV entry inhibitor maraviroc complex. Science. 2013; 341:1387–1390. [PubMed: 24030490]

Thomas WG, Baker KM, Motel TJ, Thekkumkara TJ. Angiotensin II receptor endocytosis involves two distinct regions of the cytoplasmic tail. A role for residues on the hydrophobic face of a putative amphipathic helix. J Biol Chem. 1995; 270:22153–22159. [PubMed: 7673193]

Thomas WG, Pipolo L, Qian H. Identification of a Ca2????binding domain within the carboxyl-terminus of the angiotensin II (AT1A) receptor. FEBS Lett. 1999; 455:367–371. [PubMed: 10437806]

Thompson AA, Liu W, Chun E, Katritch V, Wu H, Vardy E, Huang XP, Trapella C, Guerrini R, Calo G, et al. Structure of the nociceptin/orphanin FQ receptor in complex with a peptide mimetic. Nature. 2012; 485:395–399. [PubMed: 22596163]

Totrov M, Abagyan R. Flexible protein-ligand docking by global energy optimization in internal coordinates. Proteins-Structure Function and Genetics. 1997:215–220.

Unal H, Jagannathan R, Bhat MB, Karnik SS. Ligand-specific conformation of extracellular loop-2 in the angiotensin II type 1 receptor. J Biol Chem. 2010; 285:16341–16350. [PubMed: 20299456]

Unal H, Jagannathan R, Karnik SS. Mechanism of GPCR-directed autoantibodies in diseases. Adv Exp Med Biol. 2012; 749:187–199. [PubMed: 22695846]

Unal H, Karnik SS. Constitutive activity in the angiotensin II type 1 receptor: discovery and applications. Adv Pharmacol. 2014; 70:155–174. [PubMed: 24931196]

Weierstall U, James D, Wang C, White TA, Wang D, Liu W, Spence JC, Bruce Doak R, Nelson G, Fromme P, et al. Lipidic cubic phase injector facilitates membrane protein serial femtosecond crystallography. Nat Commun. 2014; 5:3309. [PubMed: 24525480]

Whalen EJ, Rajagopal S, Lefkowitz RJ. Therapeutic potential of beta-arrestin- and G protein-biased agonists. Trends Mol Med. 2011; 17:126–139. [PubMed: 21183406]

White TA, Kirian RA, Martin AV, Aquila A, Nass K, Barty A, Chapman HN. CrystFEL: a software suite for snapshot serial crystallography. J Appl Crystallogr. 2012; 45:335–341.

Wisler JW, Xiao K, Thomsen AR, Lefkowitz RJ. Recent developments in biased agonism. Curr Opin Cell Biol. 2014; 27:18–24. [PubMed: 24680426]

Wu B, Chien EY, Mol CD, Fenalti G, Liu W, Katritch V, Abagyan R, Brooun A, Wells P, Bi FC, et al. Structures of the CXCR4 chemokine GPCR with small-molecule and cyclic peptide antagonists. Science. 2010; 330:1066–1071. [PubMed: 20929726]

Wu H, Wacker D, Mileni M, Katritch V, Han GW, Vardy E, Liu W, Thompson AA, Huang XP, Carroll FI, et al. Structure of the human kappa-opioid receptor in complex with JDTic. Nature. 2012; 485:327–332. [PubMed: 22437504]

Xia Y, Kellems RE. Angiotensin receptor agonistic autoantibodies and hypertension: preeclampsia and beyond. Circ Res. 2013; 113:78–87. [PubMed: 23788505]

Zaman MA, Oparil S, Calhoun DA. Drugs targeting the renin-angiotensin-aldosterone system. Nat Rev Drug Discov. 2002; 1:621–636. [PubMed: 12402502]

Zhou CC, Zhang Y, Irani RA, Zhang H, Mi T, Popek EJ, Hicks MJ, Ramin SM, Kellems RE, Xia Y. Angiotensin receptor agonistic autoantibodies induce pre-eclampsia in pregnant mice. Nat Med. 2008; 14:855–862. [PubMed: 18660815]

Highlights

- Crystal structure of the human Angiotensin II type 1 receptor at 2.9 Å resolution
- Structure is solved by X-ray laser serial femtosecond crystallography
- Antagonist ZD7155 forms critical interactions with Tyr35, Trp84 and Arg167
- Docking reveals binding modes of common angiotensin receptor blockers

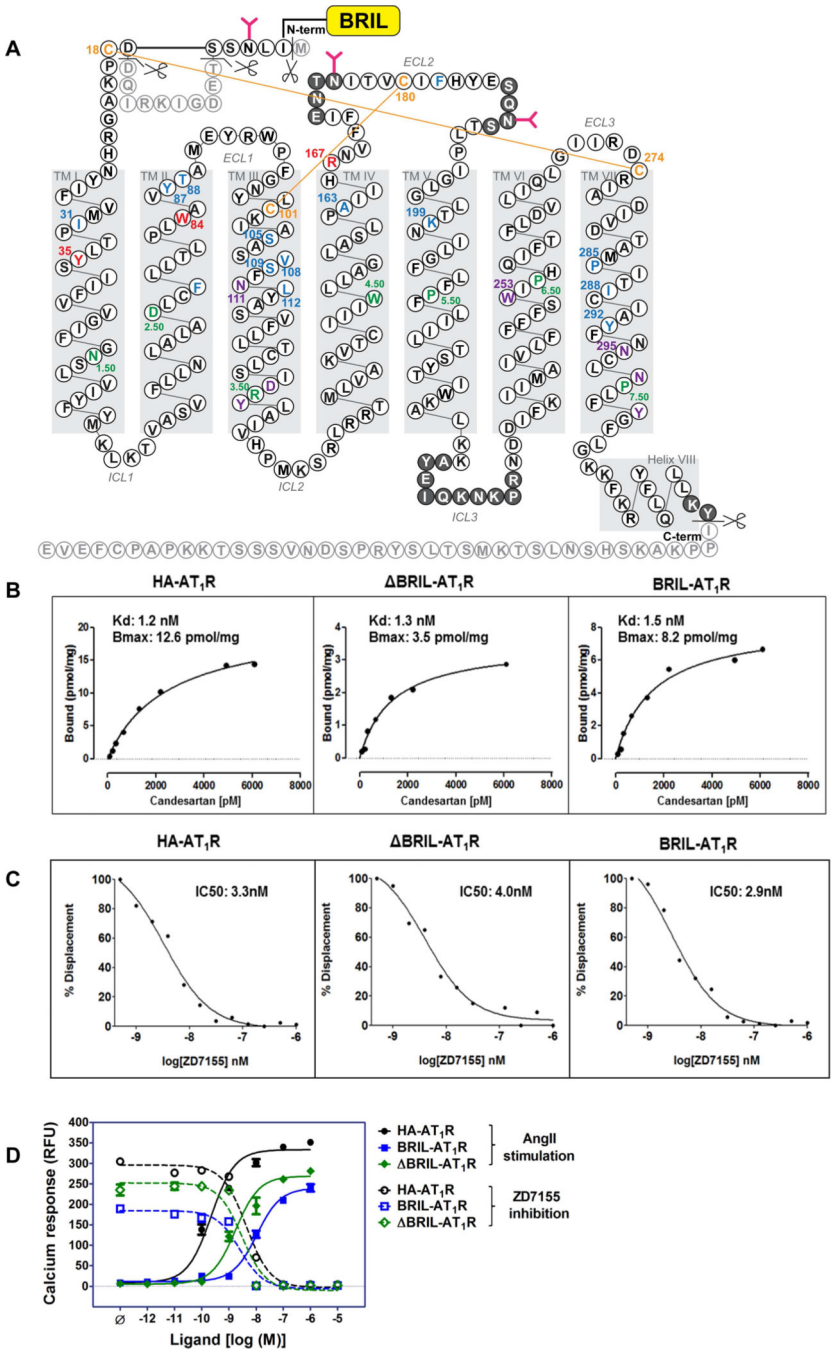

Figure 1. AT_1R construct design and functional characterization

(A) Snake plot of the BRIL-AT_1R construct used for crystallization. Residues that occupy the most conserved positions on each helix in class A GPCRs (X.50; B&W scheme) are colored in green. The four cysteine residues that form two disulfide bonds in the extracellular region are colored in orange. Three critical residues for ZD7155 binding are colored in red. All other residues that interact with ZD7155 are colored in blue. Critical residues/motifs for AT_1R activation are colored in purple. Truncated residues are shown as

light gray, and residues that do not have sufficient density in the structure and therefore were not modelled are shown in dark gray circles.

(B) Saturation binding of the non-peptide antagonist ^{3}H-candesartan to the wild type HA-AT_1R, ΔBRIL-AT_1R, and BRIL-AT_1R.

(C) Competition binding of ZD7155 to the wild-type HA-AT_1R, ΔBRIL-AT_1R, and BRIL-AT_1R, performed by displacement of ^{3}H-candesartan.

(D) Intracellular calcium responses for the wild-type HA-AT_1R, BRIL-AT_1R, and ΔBRIL-AT_1R. The agonist AngII and the antagonist ZD7155 dose-response curves for HA-AT_1R (circles), BRIL-AT_1R (squares), and ΔBRIL-AT_1R (diamonds) are shown in closed and open symbols, respectively.

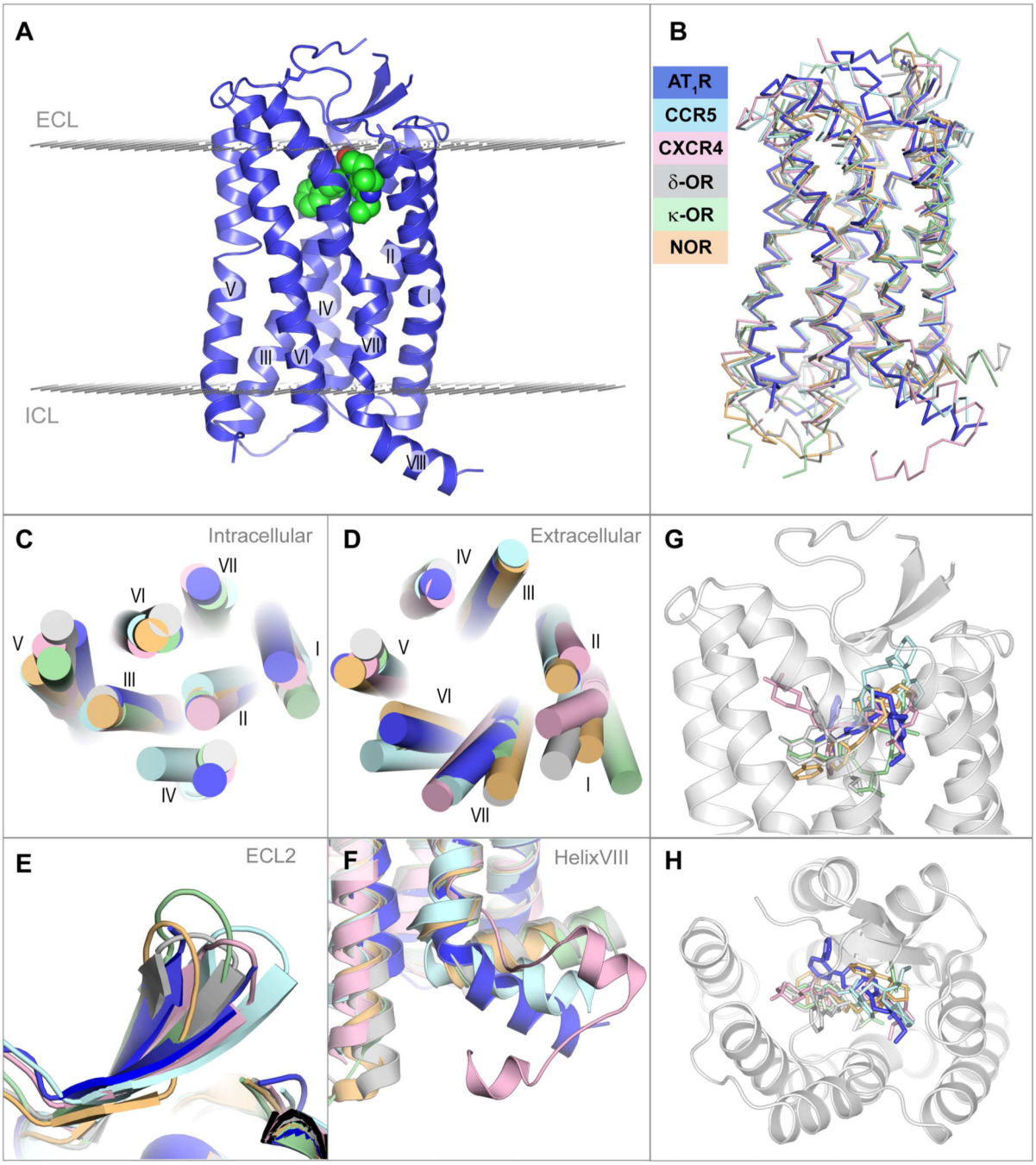

Figure 2. Overview of AT_1R-ZD7155 architecture and structural comparison with other peptide GPCRs

(A) Overall AT_1R structure is shown as blue cartoon. ZD7155 is shown as spheres with carbon atoms colored green. Membrane boundaries, as defined by the PPM web server (Lomize et al, 2012), are shown as planes made of gray spheres.

(B) – (G) superposition of AT_1R with chemokine and opioid receptors, chemokine CCR5 receptor – light cyan (PDB ID 4MBS), chemokine CXCR4 receptor – light pink (PDB ID 3ODU), δ-opioid receptor – gray (PDB ID 4N6H), κ-opioid receptor – light green (PDB ID 4DJH), NOP receptor – light orange (PDB ID 4EA3), comparing the whole structure (B),

intracellular view (C), extracellular view (D), ECL2 (E), helix VIII (F), and the ligand binding pocket side (G) and top (H) views.
See also Figures S1–S2 and Table S1.

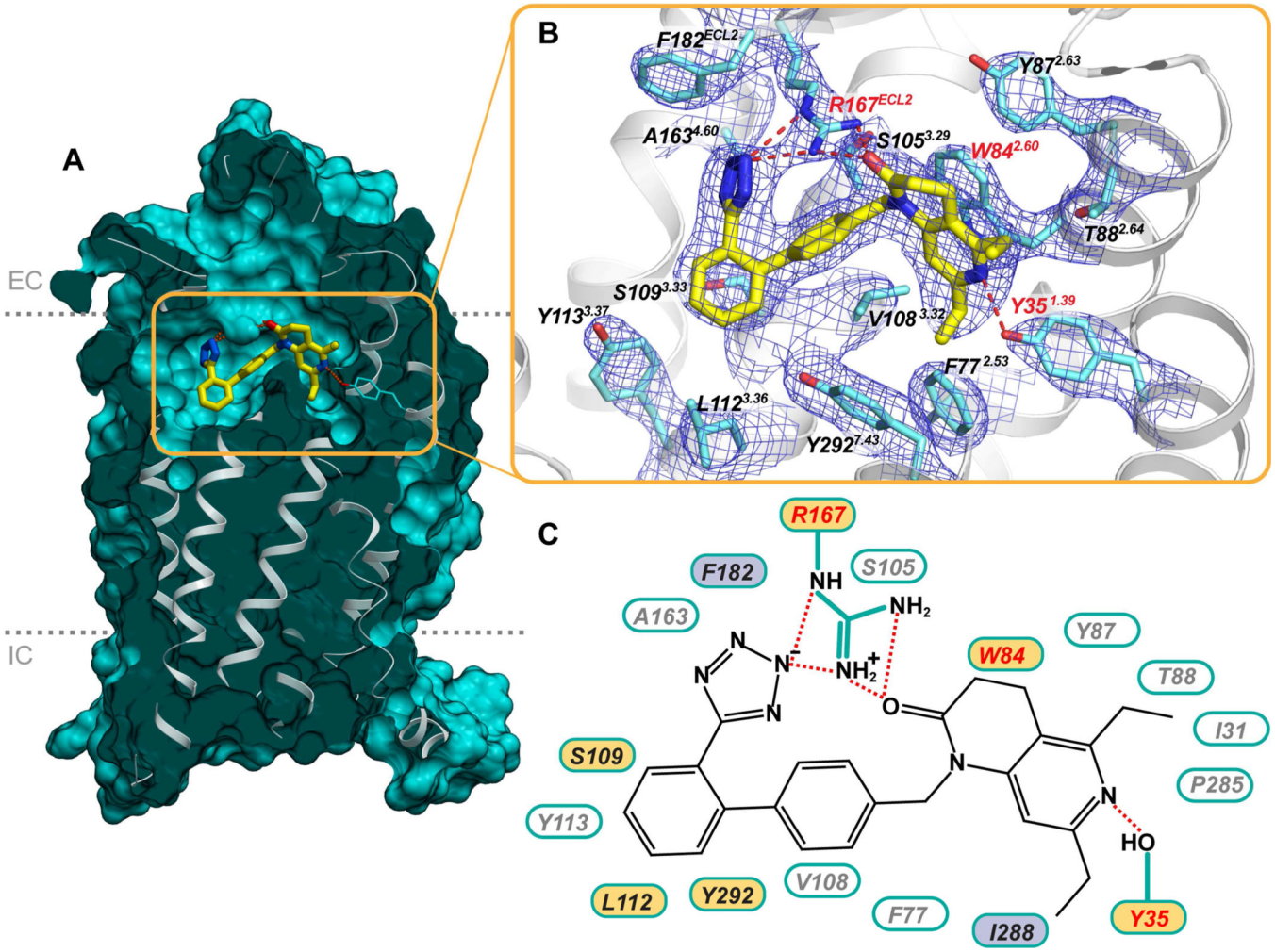

Figure 3. Interactions of ZD7155 with AT_1R

(A) Cross-section view of AT_1R highlighting the shape of the ligand binding pocket.

(B) Zoomed-in view of the ligand binding pocket showing all residues within 4 Å from the ligand ZD7155, along with the 2mFo-DFc electron density (blue mesh) contoured at 1 σ level. In (A) and (B) ZD7155 is shown as sticks with yellow carbons.

(C) Schematic representation of interactions between AT_1R and ZD7155. Hydrogen bonds/ salt bridges are shown as red dashed lines. The residues shown by mutagenesis to be critical for ligand binding are labeled red, those that are important for either peptide or non-peptide ligands binding are labeled in yellow, and the residues that discriminate between peptide and nonpeptide ligands are labeled in purple.

See also Figure S2 and Table S2.

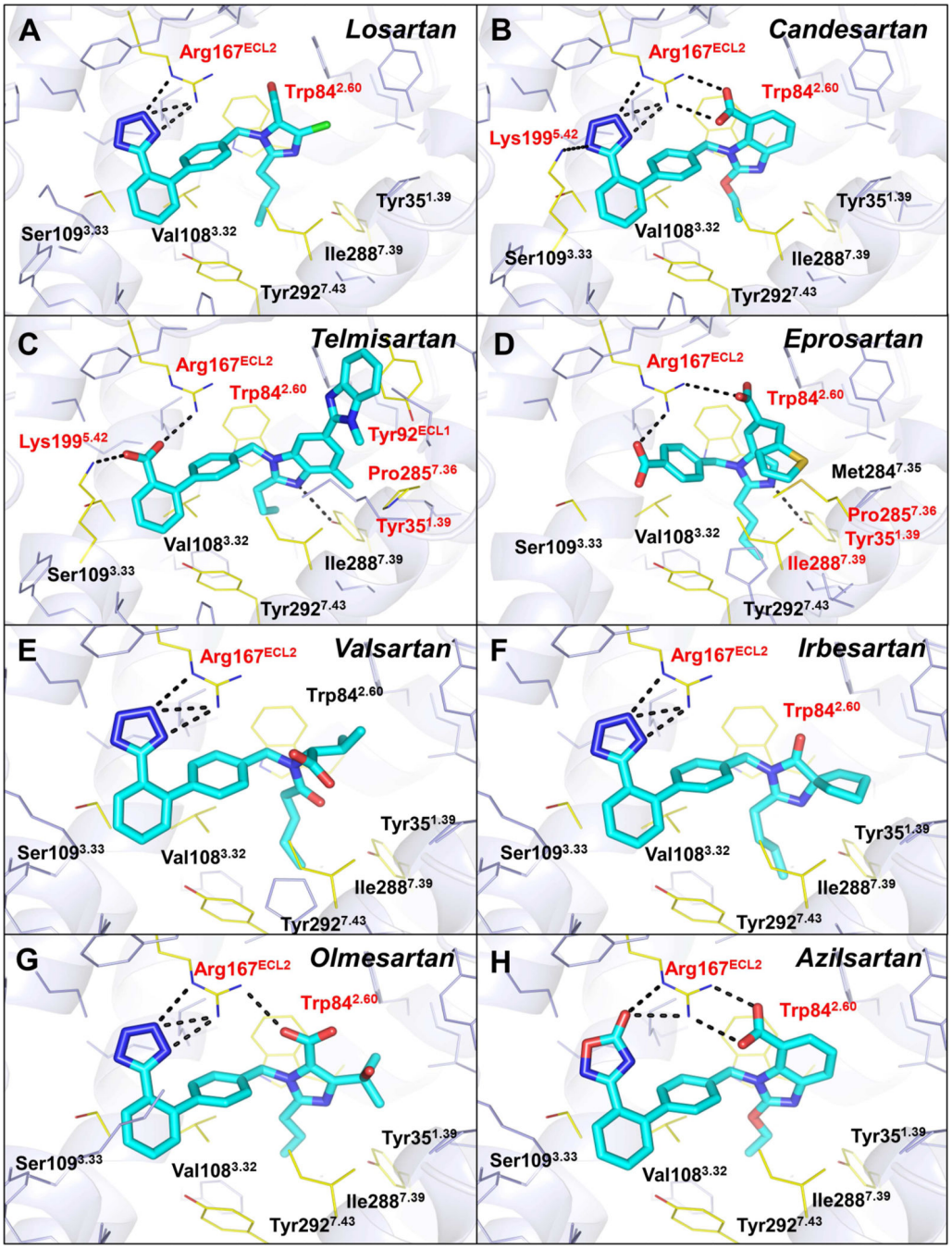

Figure 4. Docking of different anti-hypertensive drugs in the AT_1R crystal structure

The ARBs are shown as sticks with cyan carbons. The AT_1R residues interacting with ligands are labeled and shown as yellow lines, with the key residues highlighted in red. The hydrogen bonds are shown as black dashed lines.

See also Table S3.

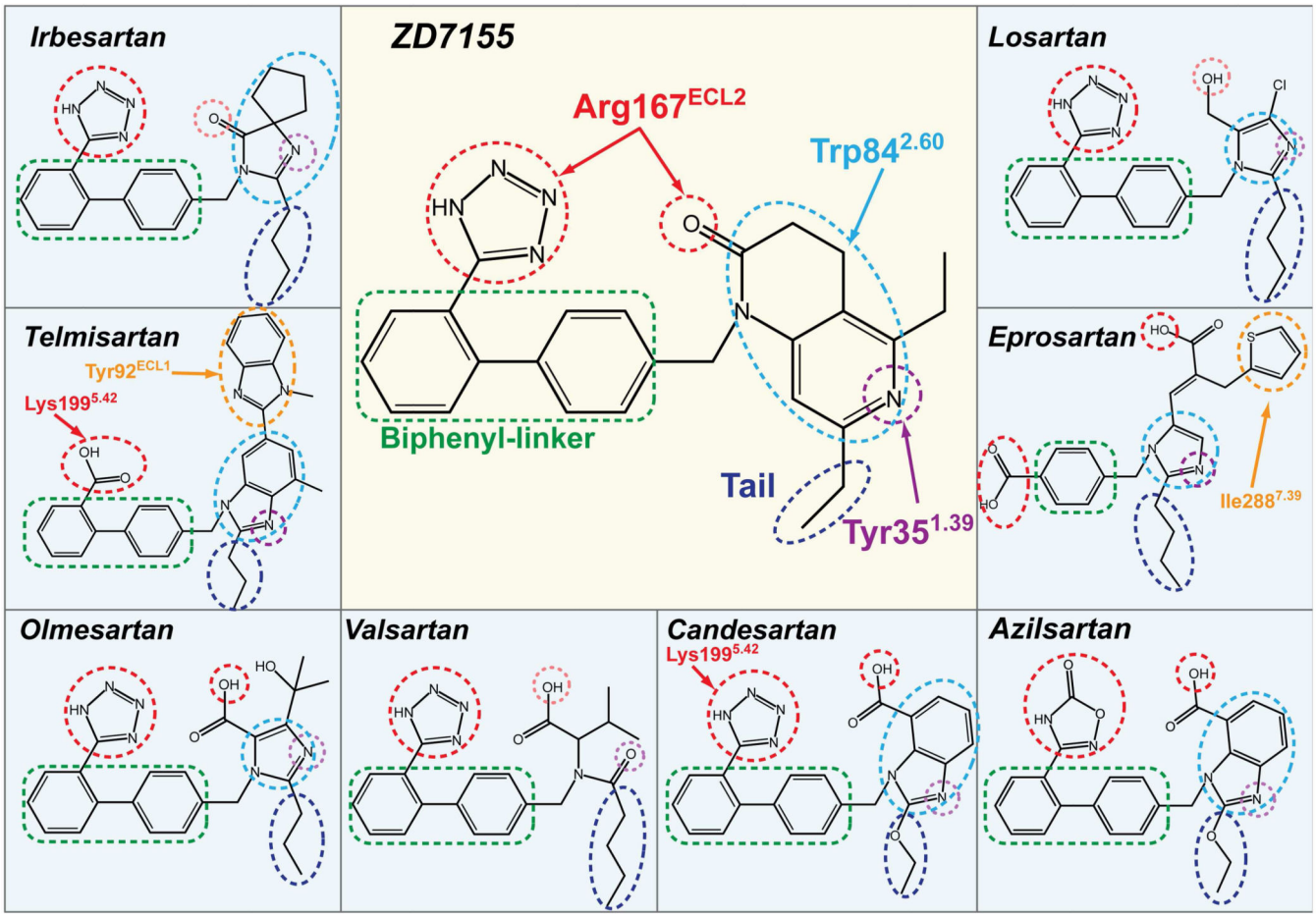

Figure 5. Common and distinct binding modes of different ARBs with AT_1R

The ARB chemical groups that are engaged in hydrogen bonding/salt bridging with $Arg167^{ECL2}$ and $Tyr35^{1.39}$ are marked by red and purple dashed circles, respectively. Pale red and pale purple dotted circles are used for groups with sub-optimal contacts as suggested by docking. The heterocyclic groups forming π-π contacts with $Trp84^{2.60}$ are surrounded by light-blue dashed circles. The biphenyl-linker groups for hydrophobic interactions are outlined by green dashed boxes, and the two-four carbons tails, extending into the hydrophobic pocket formed by $Tyr35^{1.39}$, $Phe77^{2.53}$, $Val108^{3.32}$, $Ile288^{7.39}$, and $Tyr292^{7.43}$, are outlined by dark-blue dashed circles. Specific interactions of candesartan and telmisartan with $Lys199^{5.42}$ are shown by red arrows. Specific interactions between $Tyr92^{ECL1}$ and telmisartan, and between $Ile288^{7.39}$ and eprosartan are highlighted by orange dashed circles. See also Figure S3.

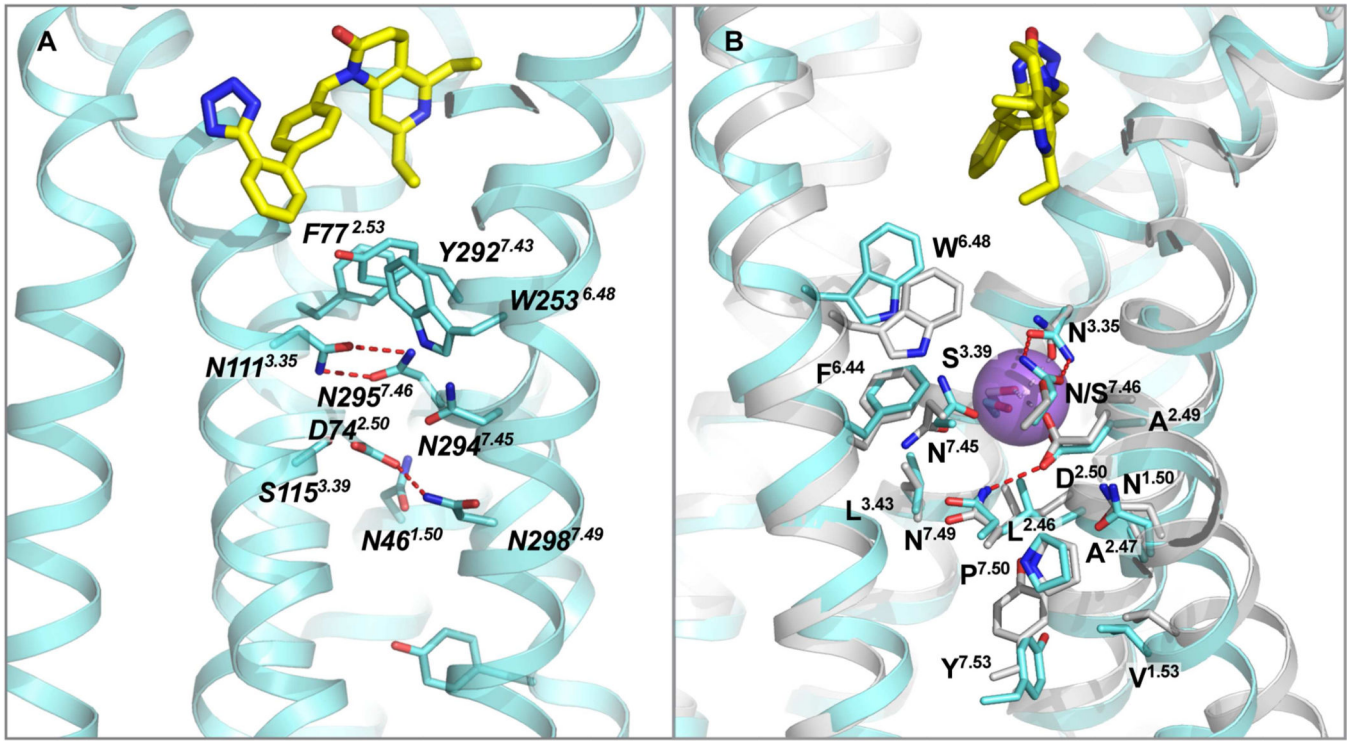

Figure 6. Critical residues for AT_1R activation

(A) A cluster of aromatic residues ($F77^{2.53}$, $W253^{6.48}$ and $Y292^{7.43}$) is located just below ZD7155, bridging the ligand binding pocket with a cluster of polar residues that includes several highly conserved in class A GPCR residues ($N46^{1.50}$, $D74^{2.50}$), along with $N111^{3.35}$ and $N295^{7.46}$ forming hydrogen bonds that hold helices III and VII together.

(B) Superposition of the AT_1R structure with the high-resolution structure of δ-OR (PDB ID 4N6H) reveals a high structural conservation of the putative sodium-binding site.